Time-dependent quantum tunneling and nonequilibrium heating model for the generalized Einstein photoelectric effect

M. Pant and L. K. Ang*

Engineering Product Development, Singapore University of Technology and Design, Singapore 138682

(Received 7 September 2012; revised manuscript received 31 October 2013; published 27 November 2013)

By combining the time-dependent Schrödinger equation with microscopic kinetic equations, a model for femtosecond-laser-induced electron emission from a metallic surface is developed to capture the physics of nonequilibrium heating and also the multiple-energy time-dependent tunneling. Using this model, we observe an enhanced electron emission due to the tranmission resonance at a particular energy level with a barrier height that produces a resonant frequency near to the laser frequency. Contrary to both pure optical tunneling and pure multiphoton emission models, the model provides better agreement with experiments. The generalized Einstein photoelectric effect is found to be inaccurate in this regime because of the nonequilibrium electron energy distribution, the resonant enhancement, and the ultrashort laser pulse width. The role of photons in the multiphoton electron emission regime is studied in detail. A smooth transition from the multiphoton regime to the optical tunneling regime is demonstrated.

DOI: 10.1103/PhysRevB.88.195434 PACS number(s): 79.70.+q, 41.75.−i, 79.20.Ws, 79.60.−i

I. INTRODUCTION

The generalized Einstein photoelectric effect predicts that the number of photons required for photoemission is an integer equal to the number of quanta that can overcome the metal work function. Also known as multiphoton electron emission, this effect is characterized by the Keldysh parameter $\gamma = \omega\sqrt{2m\Phi}/eF \gg 1$, where ω is the laser frequency, F is the electric field, and Φ is the metal work function. With recent experiments using ultrafast lasers to induce electron emission from metal tips,[1–11] it is found that classical models do not include important effects such as nonequilibrium heating, tunneling in the transition regime ($\gamma = 1$ to 10), emission from multiple energy levels, and electron acceleration due to the ponderomotive force.

In this paper, we propose a time-dependent and nonequilibrium quantum model that is able to account for the effects mentioned above and is more consistent than prior models which only cover part of the dynamical process. The prior limitations include (a) the assumption of single energy tunneling from the Fermi level while neglecting the effects of heating and emission from multiple energy levels (optical field emission),[3,7,8,12,13] (b) solving only the microscopic kinetic equations for nonequilibrium heating but using time-independent tunneling approximations (photofield emission),[5,9,14,15] and (c) studying the effect of the field gradient but ignoring both heating and time-dependent quantum tunneling.[11]

To the authors' knowledge, this is the first model which includes all the effects mentioned above. Due to the tranmission resonance,[16–18] an increment in barrier potential can actually lead to increased photoemission when the energy barrier faced by the electron is close to a multiple of the photon energy (Fig. 4) and this effect leads to peaks in the photoemitted electron energy distribution function (Fig. 5). A smooth transition from the multiphoton regime ($\gamma \gg 1$) to optical field emission ($\gamma \ll 1$) is shown in Fig. 7. Another interesting finding is that the number of photons required for photoemission deviates from that of the generalized Einstein model, which implies that the latter is no longer valid in ultrafast-laser-induced electron emission (Fig. 8). Finally, a comparison with experiment confirms that our model gives the best agreement (Fig. 9).

The system modeled here consists of a Gaussian laser pulse of duration τ, wavelength λ, and phase angle ϕ incident on a metallic tip with radius r_0 such that the laser electric field is perpendicular to the metal tip. The peak of the laser is at $t_0 = 40$ fs. In addition to the laser electric field F_0, there is a dc bias field $F_{\rm dc}$ applied at the surface of the metal in order to facilitate the transport of emitted electrons to the detector which is at a distance of 2 nm from the tip. The material has a work function Φ_m and the Fermi level is E_F. If unspecified, the values of the parameters used in this paper are $\lambda = 800$ nm, $F_0 = 3$ V/nm, $F_{\rm dc} = 0.2$ V/nm, $\tau = 20$ fs, $\phi = 0$, and $r_0 = 20$ nm. The material is tungsten with Fermi energy $E_F = 5.78$ eV and work function $\Phi_m = 4.4$ eV. The vacuum energy level $E_{\rm vac} = E_F + \Phi_m = 10.18$ eV. These default values correspond to an optical cycle of 2.67 fs. With a pulse length of 20 fs, this equals 7.5 optical cycles. As found in previous studies, the electron emission time is phase dependent and is comparable to the optical cycle.[8]

Although the model is essentially one-dimensional (1D), the values of the ac and dc electric fields at the surface (F_0 and $F_{\rm dc}$) include the field enhancement factor, and the potential profile [Eq. (10)] including the effects of a spatially decaying field is described later. Note the plasmonic effect is completely ignored.

In Sec. II, we describe the model used to calculate the photocurrent. The findings are reported in Sec. III. In Sec. IV, we discuss the assumptions used in the model, comparison with prior works, and some important issues for future works. Finally, we conclude our paper in Sec. V.

II. METHODOLOGY

The model consists of two parts: the kinetic part which determines the effect of laser heating on the electron energy distribution and the quantum tunneling part which calculates the tunneling current by solving the time-dependent

Schrödinger equation over many transmission channels which are determined from the different energy levels obtained from the kinetic part. The photocurrent as a function of time is determined by integrating over these channels.

A. Nonequilibrium heating

To account for heating, we need to obtain the nonequilibrium electron energy distribution function $f(E_e,t)$ because the pulse length of the ultrafast laser is shorter than the electron-phonon relaxation time which is several hundred femtoseconds.[19] Before the laser excitation, the electron distribution $f(E_e)$ and phonon distribution $g(E_p)$ follow the Fermi-Dirac and Bose-Einstein distributions, respectively, at room temperature. The laser excitation causes a rise in the electron energy levels. At the same time, electron-electron and electron-phonon collisions lead to a cooling effect on the electron gas which is particularly dominant after the peak of the laser pulse. Hence, the evolution of the electron and phonon energy distributions can be written as

$$\begin{aligned}\frac{\partial f(E_e)}{\partial t} &= \left.\frac{\partial f(E_e)}{\partial t}\right|_{e\text{-}e} + \left.\frac{\partial f(E_e)}{\partial t}\right|_{e\text{-}p} + \left.\frac{\partial f(E_e)}{\partial t}\right|_{\text{absorp}} \\ \frac{\partial g(E_p)}{\partial t} &= \left.\frac{\partial g(E_p)}{\partial t}\right|_{p\text{-}e},\end{aligned} \tag{1}$$

where e-e represents the effect of electron-electron collisions, e-p and p-e represent the effects of electron-phonon collisions, and absorp represents the effect of laser energy absorption.

Based on first-order perturbation theory, we have[14,15,20]

$$\begin{aligned}\left.\frac{\partial f(k)}{\partial t}\right|_{e\text{-}e} &= \frac{2\pi}{\hbar}\sum_{\boldsymbol{k}_1,\boldsymbol{k}_2,\boldsymbol{k}_3}|M_{ee}|^2 F(\boldsymbol{k},\boldsymbol{k}_1,\boldsymbol{k}_2,\boldsymbol{k}_3) \\ &\times \delta(\boldsymbol{k}+\boldsymbol{k}_1-\boldsymbol{k}_2-\boldsymbol{k}_3) \\ &\times \delta[E(k)+E(k_1)-E(k_2)-E(k_3)],\end{aligned} \tag{2}$$

where $F(\boldsymbol{k},\boldsymbol{k}_1,\boldsymbol{k}_2,\boldsymbol{k}_3) = -f(\boldsymbol{k})f(\boldsymbol{k}_1)[1-f(\boldsymbol{k}_2)][1-f(\boldsymbol{k}_3)] + f(\boldsymbol{k}_2)f(\boldsymbol{k}_3)[1-f(\boldsymbol{k})][1-f(\boldsymbol{k}_1)]$ represents the possible energy transitions of the electrons and $\delta(\boldsymbol{k}+\boldsymbol{k}_1-\boldsymbol{k}_2-\boldsymbol{k}_3)$ and $\delta[E(k)+E(k_1)-E(k_2)-E(k_3)]$ represent momentum and energy conservation, respectively. The interaction matrix M_{ee} is based on a screened Coulomb potential given by

$$\begin{aligned}|M_{ee}|^2 &= \left[\frac{e^2}{\epsilon_0 V}\frac{1}{\Delta k^2+\kappa_{\text{sc}}^2}\right]^2, \\ \text{where } \kappa_{\text{sc}}^2 &= \frac{e^2 m_e}{\pi^2\hbar^2\epsilon_0}\int_0^\infty f(k)dk.\end{aligned} \tag{3}$$

Here, $\Delta\boldsymbol{k} = \boldsymbol{k}_1-\boldsymbol{k}_2 = \boldsymbol{k}_3-\boldsymbol{k}$ is the scattering transferred momentum and κ_{sc} (Ref. 20) is the static screening length which is calculated at each time step. Note, m_e is the effective mass of a free electron in the conduction band.

The electron-phonon interaction contributions are given by

$$\begin{aligned}\left.\frac{\partial f(k)}{\partial t}\right|_{e\text{-}p} &= \frac{2\pi}{\hbar}\sum_{\boldsymbol{q}}|M_{ep}|^2\{S^-(\boldsymbol{k},\boldsymbol{q}) \\ &\times \delta[E(k)-E(k^-)-E_{\text{ph}}(q)] \\ &+ S^+(\boldsymbol{k},\boldsymbol{q})\times\delta[E(k)-E(k^+)+E_{\text{ph}}(q)]\},\end{aligned} \tag{4}$$

$$\begin{aligned}\left.\frac{\partial g(q)}{\partial t}\right|_{p\text{-}e} &= 2\times\frac{2\pi}{\hbar}|M_{ep}|^2\sum_{\boldsymbol{k}}S^+(\boldsymbol{k},\boldsymbol{q}) \\ &\times\delta[E(k)-E(k^+)+E_{\text{ph}}(q)],\end{aligned} \tag{5}$$

where $S^-(\boldsymbol{k},\boldsymbol{q}) = f(\boldsymbol{k}^-)[1-f(\boldsymbol{k})]g(\boldsymbol{q}) - f(\boldsymbol{k})[1-f(\boldsymbol{k}^-)][1+g(\boldsymbol{q})]$ and $S^+(\boldsymbol{k},\boldsymbol{q}) = f(\boldsymbol{k}^+)[1-f(\boldsymbol{k})][1+g(\boldsymbol{q})] - f(\boldsymbol{k})[1-f(\boldsymbol{k}^+)]g(\boldsymbol{q})$. $\boldsymbol{k}^+ = \boldsymbol{k}+\boldsymbol{q}$ and $\boldsymbol{k}^- = \boldsymbol{k}-\boldsymbol{q}$ are the possible transitions of the electron wave vector with the absorption and emission of a phonon.

If the phonon energy is $E_{\text{ph}}(q) = \hbar v_s q$ and v_s is the speed of longitudinal phonons, the interaction matrix is given by

$$|M_{ep}|^2 = \frac{1}{2\epsilon_0 V}\frac{e^2}{q^2+\kappa_{\text{sc}}^2}E_{\text{ph}}(q). \tag{6}$$

Finally, the laser perturbation is described by

$$\begin{aligned}&\left.\frac{\partial f(k)}{\partial t}\right|_{\text{absorp}} \\ &= \frac{2\pi}{\hbar}\sum_{\boldsymbol{q}}|M_{ep}|^2\sum_l J_l^2\left(\frac{e\boldsymbol{F}_{\text{laser}}\cdot\boldsymbol{q}}{m_e\omega^2}\right) \\ &\times\{S^-(\boldsymbol{k},\boldsymbol{q})\times\delta[E(k)-E(k^-)-E_{\text{ph}}(q)+l\hbar\omega] \\ &+ S^+(\boldsymbol{k},\boldsymbol{q})\times\delta[E(k)-E(k^+)+E_{\text{ph}}(q)+l\hbar\omega]\},\end{aligned} \tag{7}$$

where ω is the laser frequency and F_{laser} is the laser field. The heating process is assumed to be isotropic.

Using the nonequilibrium heating model described above, the time-dependent electron energy distribution $f(E_e,t)$ is calculated as shown in Fig. 1. From the figure, we see that $f(E_e,t)$ starts with a Fermi-Dirac distribution at $t = 0$ fs, and a steplike profile appears at a later time, which is characteristic of nonequilibrium heating and one step size corresponds to the energy of a photon absorption. The evolution continues until a maximum at $t_0 = 40$ fs (blue line), which is at the peak of the laser pulse. After 40 fs, the distribution starts to drop (due to the decreasing of the laser intensity) and reaches a new quasiequilibrium Fermi-Dirac distribution with a higher temperature as seen at 60 fs (pink line).

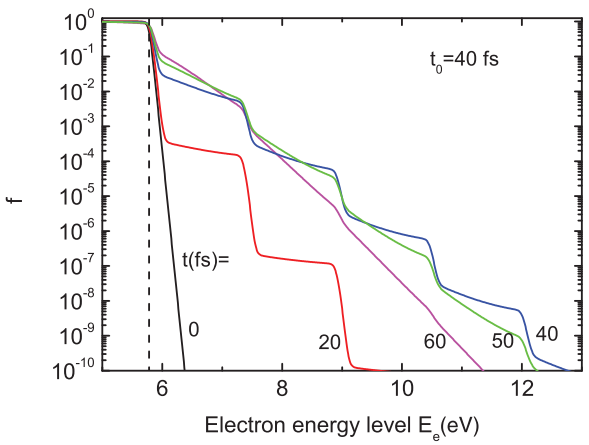

FIG. 1. (Color online) Evolution of the nonequilibrium electron energy distribution f with time. The vertical dashed line represents the Fermi level E_F.

To determine the amount of electron tunneling from the a surface to vacuum (for multiple energy channels, which vary with time), we calculate the time-dependent electron density $N(E_x,t)$ with energy E_x in the x direction (normal to the surface). From the calculated $f(E_e,t)$ as shown in Fig. 1, $N(E_x,t)$ is calculated by

$$N(E_x,t)dE_x = \left(\frac{me}{2}\right)^{3/2} dE_x/\pi^2\hbar^3\sqrt{E_x}\int_{E_x}^{\infty} f(E_e)dE_e, \tag{8}$$

which can be considered as the time-dependent electron supply function as normally defined in the electron emission model.

It is important to note that the energy parameter E_x in $N(E_x,t)$ also changes as a function of time, which is at the femtosecond time scale comparable to the tunneling time, so a multiple-energy time-dependent tunneling model is required to include the time evolution of the electron energy $E_x(t)$. A numerical scheme has been created to calculate $E_x(t)$ [see Eq. (9) below]. Consider electrons with initial energy E_0 at $t = 0$, due to the nonequilibrium laser heating (see Fig. 1), the electrons will have higher energy $E_x(t)$ at a later time. As the number of electrons for a given initial energy E_0 is a constant, we obtain a relation of $N[E_x(t),t] = N(E_0,0)$, from which we can infer that the energy of the electron is (as a function)

$$E_x(E_0,t) = N^{-1}[N(E_0,0),t], \tag{9}$$

and the function $N(E_0,0)$ is calculated from Eq. (8).

In Fig. 2, we plot $E_x(E_0,t)$ for various $E_0 = 3.6$ to 6.1 eV. For low $E_0 = 3.6$ eV, the electron energy is fairly constant. For high $E_0 > 5.78$ eV, which is larger than the Fermi energy level ($E_F = 5.78$ eV), E_x shows a steplike profile due to the quantization of photon absorption, and it decreases gradually after the peak of the laser pulse at 40 fs. The horizontal and vertical dashed lines indicate, respectively, the Fermi energy $E_F = 5.78$ eV and the peak of the laser pulse at 40 fs. As expected, electrons gain energy during the initial part of the pulse and gradually cool down after the peak of the laser pulse.

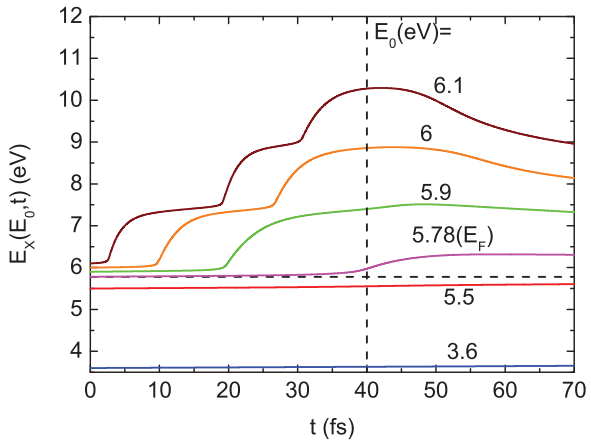

FIG. 2. (Color online) Evolution of the electron energy for different initial energies E_0. The vertical dashed line represents t_0 and the horizontal dashed line represents the Fermi level E_F.

B. Multienergy time-dependent tunneling

In the second part of the model, we use the calculated $E_x(E_0,t)$ to solve for the time-dependent Schrödinger equation (TDSE) to calculate the total time-dependent current density $J(t)$ over all channels and also the time-integrated emitting charge density σ. Depending on the initial energy level E_0, the electrons will have different energies as a function of time, which are obtained by solving $E_x(E_0,t)$ or Eq. (9) numerically. For each E_0, we may define a transmission channel in the sense that all electrons with the same E_0 will have the same tunneling probability since the time evolution of $E_x(E_0,t)$ has been determined by Eq. (9). To ensure our calculations cover the entire range of energy levels, we have used a very fine sampling of $E_0 = 0$ to 6.6 eV to define our transmission channels in our model, so that we can calculate the evolution of the wave function of these electrons. Specifically, one time-dependent Schrödinger equation is solved for each transmission channel, and in total, we typically solve about 150 of them for a given set of parameters.

Consider the metal-vacuum interface at $x = 0$, the time-dependent potential energy outside the metal ($x \geqslant 0$) due to the laser is

$$\begin{aligned} U(x,t) = {} & E_{\rm vac} - \frac{e^2}{16\pi\epsilon_0(x+x_0)} \\ & - e\left\{F_{\rm dc}x + F_0 x\exp\left(-2\ln 2\frac{(t-t_0)^2}{\tau^2}\right)\right. \\ & \left.\times\cos[\omega(t-t_0)+\phi]\right\} \\ & \times\left[(1/2)\frac{r_0}{x}\left(1-\frac{1}{(x/r_0+1)^2}\right)\right], \end{aligned} \tag{10}$$

where $E_{\rm vac}$ is the vacuum energy level, $\omega = 2\pi c/\lambda$ is the laser angular frequency, $x_0 = e/[16\pi\epsilon_0 E_{\rm vac}]$ (for continuity), and $t_0 = 40$ fs is a reference point at the center of the laser pulse. The second term is the classical image charge term and the next term represents the electric field ($F_{\rm dc}$ and F_0). The last term in Eq. (10) accounts for the effects of the spatially dependent laser electric field near the tip: $F(x) \approx F \times [r_0/(x+r_0)]^3$, under the assumptions that the beam waist is large as compared to the barrier width and the tip has a large geometric field enhancement,[11] both of which are valid in almost all experimental studies.[2–9,11,21] Note we have used a classical image charge term similar to the one used in previous studies [second term in Eq. (10)].[3,13] As a reference point, we have defined the $E_{\rm vac}$ such that the $E_{\rm vac} - \Phi_m = 0$.

It should be noted that the laser field (F_0) specified in Eq. (10) is the peak envelope of the laser field measured at the surface of the metal. While the spatial dependence caused by the tip radius has been taken into account in the last term of Eq. (10), we did not explicitly calculate the field enhancement factor separately, which we have assumed to be included in the specified value of F_0 used in the calculation. In other words, the field enhancement factor has been included at the zero-order approximation in this 1D model.

To solve for the TDSE at a given channel, we need to know the initial wave function at $t = 0$ with energy E_0. To do so, we solve for the time-independent Schrödinger equation in the

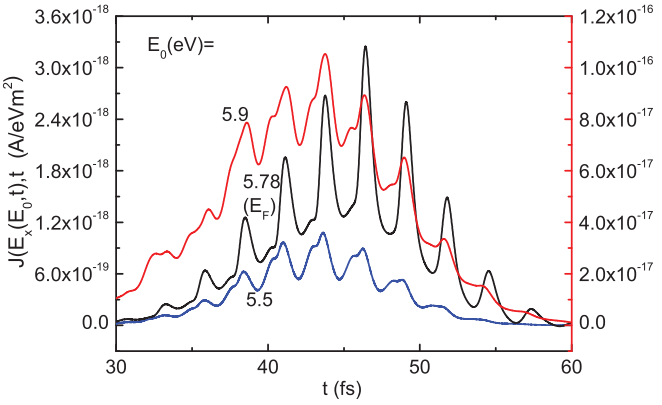

FIG. 3. (Color online) The time- and energy-dependent emission current density $J[E_x(E_0,t),t]$ for channels with different E_0. The blue and black lines use the left y axis and the red line uses the right y axis.

absence of any external fields, which gives

$$\Psi_0(x<0) = C_1\sin(k_m x) + C_2\cos(k_m x),$$
$$\Psi_0(x>0) = C_3 W_{a/2\sqrt{b},-1/2}[2\sqrt{b}(x+x_0)], \quad (11)$$

where $k_m = \sqrt{2mE_0}/\hbar$, $W_{k,m}(x)$ is the Whittaker W function, $a = e^2m/(8\hbar^2\pi\epsilon_0)$, and $b = 2(E_{\rm vac}-E_0)/\hbar^2$.

In addition to the acceleration and tunneling of the electrons by the laser field, the potential barrier is also lowered by the increase in electron energy due to laser heating. Hence, the potential energy as a function of time becomes $U(x,t) - [E_x(E_0,t) - E_0]$ due to heating. For a given E_0, we first calculate $E_x(E_0,t)$ from Eq. (9) and then solve the TDSE with $U(x,t) - [E_x(E_0,t) - E_0]$ (due to heating) to calculate the wave function as a function of position and time. From these solutions of TDSE calculated for each E_0, we can obtain the time- and energy-dependent emission current density defined as $J[E_x(E_0,t),t]$, which is determined from the wave functions at 2 nm from the surface of the metal.

A typical profile of $J[E_x(E_0,t),t]$ is plotted in Fig. 3 for $E_0 = 5.5$, 5.78 (Fermi energy level), and 5.9 eV. The total time-dependent current density is calculated by integrating over all channels: $J_{\rm tot}(t) = \int N(E_x)J(E_x,t)dE_x$ (see Fig. 6). The time-integrated emitted charge density (σ) can also be calculated by integrating $J_{\rm tot}$ over the entire laser pulse length (see Fig. 7).

III. RESULTS

In this section, we first show that the effect of the transmission resonance that has been observed in gas ionization[16,17] is also possible for the ultrafast laser electron emission studied in this paper. The emitted charge density σ (calculated by integrating $J_{\rm tot}$) at a single channel energy is plotted in Fig. 4(a) as a function of the barrier height $E_b = E_{\rm vac} - E_x$. The figure shows that σ decreases with increasing E_b, but there are distinct localized peaks corresponding to the transmission resonances. Taking into account the lowering of the potential barrier by the dc bias, these peaks appear when the effective barrier height $(E_b - E_{\rm dc})$ is equal to the energy of N photons or $E_b = N\times h\nu + E_{\rm dc}$, where $h\nu$ is the photon energy, $E_{\rm dc}$ is

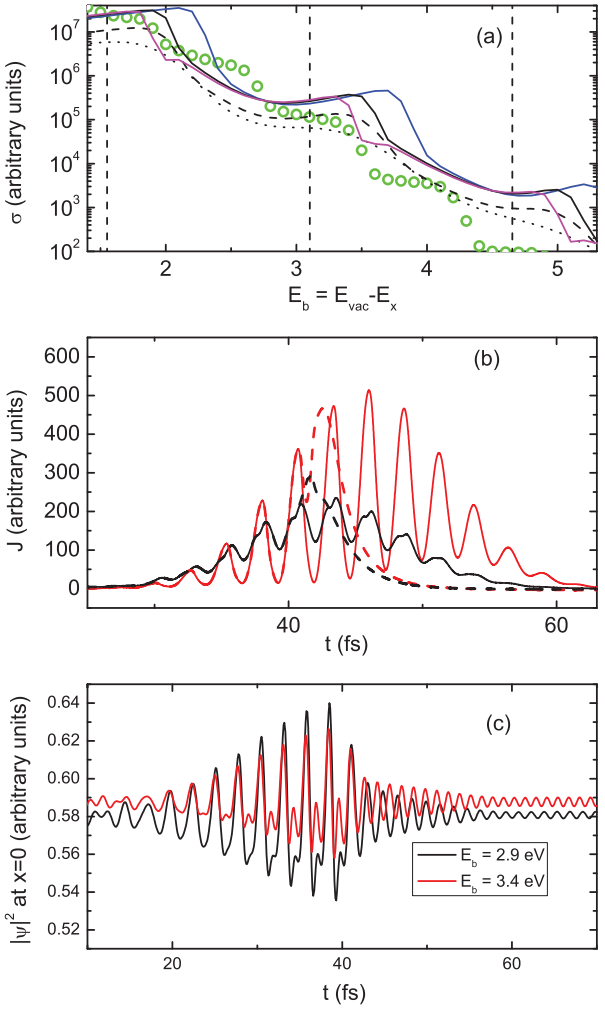

FIG. 4. (Color online) (a) Emitted charge as a function of the energy barrier with different parameters: $F_{\rm dc}$ [V/nm] = 0.1 (pink line), 0.2 (black line), and 0.4 (blue line), laser pulse widths $\tau = 20$ fs (solid lines), 8 fs (dashed line), and 4 fs (dotted line). $\lambda = 800$ nm in all cases except the green circles which correspond to $\lambda = 1600$ nm. The Keldysh parameter γ is between 3.1 and 9. The vertical dashed lines are multiples of the photon energy. (b) Comparison of the current vs time curve for $E_b = 2.9$ eV (black lines) and 3.4 eV (red lines). The solid lines represent the case of the full laser pulse while the laser and dc field are turned off near the middle of the pulse for the dashed lines. (c) Plot of the probability density at the metal surface at two different values of E_b corresponding to the dotted lines in Fig. 4(b).

the lowering of the barrier by the dc field, and $N = 1,2,\ldots$ is an integer.

Here, the peaks (or resonance transmissions) occur when the effective barrier height $(E_b - E_{\rm dc})$ is equal to the energy of N photons. At 800 nm and $F_{\rm dc} = 0.2$ V/nm (black solid line), we have $h\nu = 1.55$ eV and $E_{\rm dc} \approx 0.3$ V, and the three peaks ($N = 1$, 2, and 3) are at $E_b \approx 1.85$, 3.4, and 4.95 eV, respectively, as shown in the figure. By changing $F_{\rm dc} = 0.1$ V/nm (pink) and 0.4 V/m (blue), the peaks will be shifted slightly to new E_b due to the difference in $E_{\rm dc}$. From Eq. (10), we can see that the magnitude of the peak shift is similar to the lowering of the barrier by $F_{\rm dc}$. Interesting, the resonance is found to become less important at small τ for

which the peaks become less prominent when τ is reduced from 20 fs (solid line) to 8 fs (dashed line) to 4 fs (dotted line).

Because of the peaks, an increase in the barrier height can actually increase photoemission. For example σ at $E_b = 3.4$ eV is much higher than $E_b = 2.9$ eV [see the black solid line in Fig. 4(a)]. To explain this, the emitted current density $J(t)$ is plotted in Fig. 4(b) for $E_b = 2.9$ eV (black) and 3.4 eV (red), respectively. The corresponding dotted lines have identical parameters except that both the laser field and the dc field are turned off at the time when the laser field returns to zero after the peak laser field at 40 fs. From the figure, it is clear that the emitted current persists even after the fields are turned off. From the wave functions obtained from solving the TDSE, we realize that the laser field sets up oscillations in the wave function. In Fig. 4(c), the probability density at the metal surface with two different values of E_b is plotted corresponding to the dotted lines in Fig. 4(b); i.e., the fields are turned off after the center peak. The oscillations can be clearly seen in Fig. 4(c) with a frequency equal to the laser frequency before $t_0 = 40$ fs.

Once the fields are turned off, the oscillations persist and they settle at their *natural* frequency, which is about E_b/h and is independent of the laser frequency used. At $E_b = 3.4$ eV, we have $E_b/h \approx 820$ THz, which is very close to the 800 THz obtained from direct observation of the wave function as a function of time near the surface [see the oscillation after $t > 40$ fs, Fig. 4(c)]. The measured frequency is within 3% of E_b/h for E_b once the oscillations attain their natural frequency. Thus, when the effective barrier equals a multiple of the photon energy, i.e., E_b (at the peak)$-E_{\rm dc} = N \times h\nu$, this natural oscillation frequency matches the frequency of the laser field, which provides the enhancement in the oscillation amplitude and explains the localized peaks in Fig. 4(a).

These oscillations require a finite time to be set up and, hence, the resulting current is slightly delayed as shown in Fig. 4(b). At the beginning of the pulse (<40 fs), the lower barrier case (2.9 eV, black line) has a higher current because oscillations for the higher barrier case (3.4 eV, red line) have not started yet, for which they become dominant only at a longer time later ($t > 40$ fs). This finite delay time explains why the peaks become less prominent at shorter pulse lengths (not enough time to set up the oscillation) from $\tau = 20$ to 8 fs (dashed line) to 4 fs (dotted line) as observed in Fig. 4(a). Similarly, if we increase the wavelength λ from 800 to 1600 nm (symbols), the peaks also become smaller due to the same effect. The corresponding number of laser periods for the three cases of smaller peaks (dashed line, dotted line, and symbols) are $f\tau = 3$, 1.5, and 3.75, which are smaller than $f\tau = 7.5$ at $\lambda = 800$ nm and $\tau = 20$ fs (solid line). Thus we predict that such resonance transmission will require a finite laser period on the order of 10.

In Fig. 5, the photoemitted electron energy distribution function $f_{\rm emit}(E_x) = \int N(E_x,t)J(E_x,t)dt$ is plotted in order to show the relative contributions of different energy levels. The figure shows that the peak emission is not from the Fermi level as is generally assumed in other works. The peaks in the emission spectrum are separated by a photon energy of 1.55 eV (800 nm) or 2.25 eV (550 nm), which represents the energy corresponding to the resonance transmission discussed earlier. For example, the peak at $E_b = 4.95$ eV for 800 nm

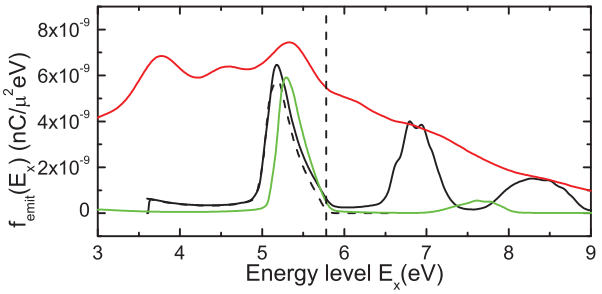

FIG. 5. (Color online) Spectrum of the emitted charge density for different laser parameters. The black solid line represents $\lambda = 800$ nm and $\tau = 20$ fs. The other plots are F_0 changed from 3 to 30 V/nm (red line), λ changed from 800 to 550 nm (green line), and $f(E_e)$ equal to the Fermi-Dirac distribution, i.e., no heating but multiple electron energies (dashed line). The vertical dashed line represents the Fermi level.

in Fig. 4(a) is seen here as the $N = 3$ photon absorption at an energy equal to $E_x = E_{\rm vac} - N \times h\nu - E_{\rm dc} = 5.23$ eV as shown by the first peak in Fig. 5. When heating is turned off, $f(E_e)$ is equal to the Fermi-Dirac distribution (dashed line), and the two peaks at energy higher than E_F disappear [see dashed lines in Fig. 5], which confirms the importance of having heating in order to describe accurately the multiphoton electron emission due to the ultrafast laser. A comparison at 550 nm (green line) is also plotted. At high $F_0 = 30$ V/nm (red line) in the optical tunneling regime, the spectrum broadens as tunneling becomes more dominant than the multiple photon absorption as expected.

As mentioned, the importance of heating cannot be ignored as it will also strongly affect the amount of emitted current. As expected, heating leads to a higher current and the effect of heating is more apparent at larger pulse width. With a 20 fs pulse, the photocurrent with heating included is 2.4 times greater than when heating is ignored, but with an 8 fs pulse this ratio is reduced to 1.8 as can be seen in Fig. 6.

In Fig. 7, we show the emitted charge density σ as a function of the laser field F_0 in the range of 3 to 50 V/nm, from the multiphoton regime ($F_0 \approx 3$ V/nm) to the optical tunneling regime ($F_0 > 10$ V/nm) with $\lambda = 800$ nm and $\tau = 20$ fs as default parameters. Our model does not produce the unphysical fluctuations shown by single energy models (pink line)[12,13] at $F_0 > 10$ V/nm (optical tunneling regime) and also gives a smooth transition consistent with experimental findings.[7]

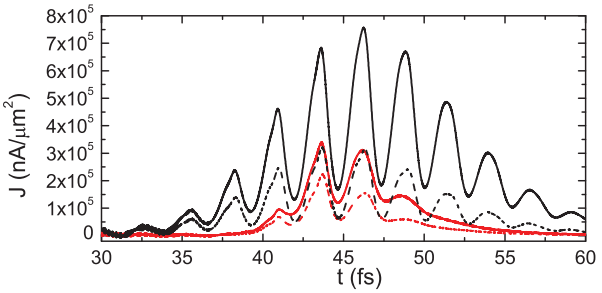

FIG. 6. (Color online) Comparison of the current vs time graph with (solid line) and without (dashed line) heating for pulse lengths of 20 fs (black lines) and 8 fs (red lines).

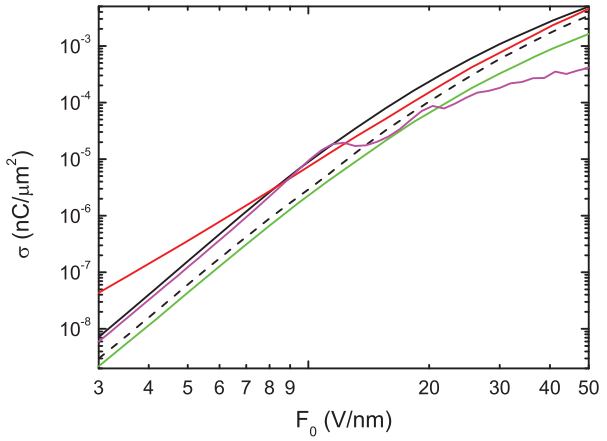

FIG. 7. (Color online) Dependence of emitted charge density σ on F_0 for different laser parameters. The black solid line is the combined model with $\lambda = 800$ nm and $\tau = 20$ fs (default case). The pink and dashed black lines represent the single energy model and the no-heating case, respectively, with the same parameters. λ is changed to 550 nm for the red line and τ is reduced to 8 fs for the green line. A smooth transition into the tunneling regime is seen as observed experimentally.

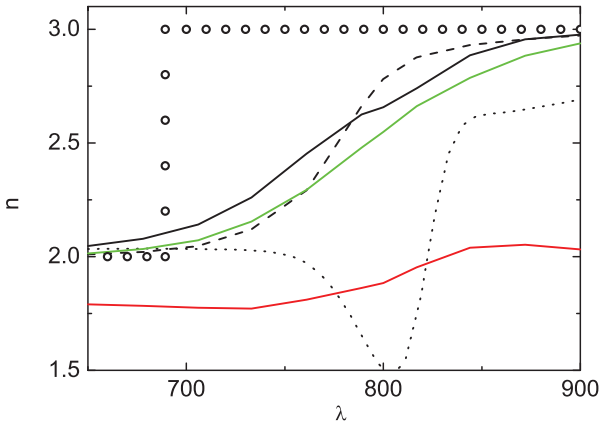

FIG. 8. (Color online) Dependence of the order of the multiphoton emission process n on the laser wavelength λ under different conditions, where n is calculated from the scaling of $\sigma \propto F_0^{2n}$ from Fig. 7. The black solid line is the combined model with $\lambda = 800$ nm and $\tau = 20$ fs (default case). The dashed and dotted black lines represent, respectively, the multiple energy without heating case and the single energy without heating case, with the same parameters. The green line represents the default case with a smaller $\tau = 8$ fs. The circles represent the generalized Einstein photoelectric effect. The red line represents n_E.

Comparisons under different settings are also plotted: 550 nm (red line), 8 fs (green line), and without heating (dashed line).

The number of photons incident on the metal is proportional to the laser intensity or F_0^2. For n number of photon absorption, the process should be of order n, and thus the emitted charge density should scale as $\sigma \propto F_0^{2n}$. From Fig. 7, we obtain the value of n photon absorption (in the multiphoton regime) by using a fitting of $\sigma \propto F_0^{2n}$ at $F_0 = 3$ V/nm. In other words, n is simply half the slope of the $\log(\sigma)$ vs $\log(F_0)$ calculated at around $F_0 = 3$ V/nm in the figure. In may be worth mentioning that such a method has been used to estimate the average number of photon absorption for electron emission by fitting the experimental measured data[7] with such scaling.

In Fig. 8, the value of n is plotted as a function of λ at $\tau = 20$ fs (in black) for three different scenarios: multiple energy with (solid line) and without (dashed line) heating, and also single energy at E_F (dotted line). We have chosen a work function of $\Phi_m = 3.6$ eV for reasons that will be explained shortly. Unlike the generalized Einstein photoelectric effect (circles), which predicts an abrupt jump from $n = 2$ to 3 at $\lambda = 689$ nm, our model shows a smooth transition in the range of 689 to 900 nm. Compared to the single energy case (dotted line), the wavelength λ at the transition ($n = 2$ to 3) for both multiple energy with (solid line) and without (dashed line) heating cases shifts to smaller λ because the majority of the electron emission (from both cases) is from energy smaller than E_F (see Fig. 5). Comparison with a smaller $\tau = 8$ fs is also plotted (green line).

We use $\Phi_m = 3.6$ eV (magnesium) in Fig. 8 because it gives $\lambda = 800$ nm (in the middle of the transition from $n = 2$ to 3), which is suitable if the model is to be verified by using a femtosecond pulsed Ti:sapphire laser. By shining an 800 nm laser on a material with $\Phi = 3.6$ eV, it should be possible to observe the transition between $n = 2$ and $n = 3$ as predicted by this paper. If a work function of $\Phi_m = 4.4$ eV (gold or tungsten), the wavelength of the transition will be around 670 nm.

It is interesting that even though a significant portion of the electron emission is from energies greater than E_F (see Fig. 5), this does not translate into a significant reduction in photon absorption n. In the traditional understanding, we expect a small number of photons are required if the energy of the electrons is increased since the barrier will be smaller. To explain this, we need to study the contribution of n in more detail, namely, the value of n can be divided into two parts: $n = n_H + n_E$, where n_H is due to the heating effect and n_E is due to the absorption of photons at each energy level.

In order to separate n_E from the total n, we assume a constant $N(E_x,t)$ [to ensure no heating] in calculating the slope of $\log(\sigma)$ vs $\log(F_0)$. Specially, in calculating the slope of Fig. 7, we take two points close to 3 V/nm. For n_E (no heating), we only calculate $N(E_x,t)$ at one of the two points and use it as an input to calculate the emitted charge at both points. In doing so, we are able to calculate n_E, which is not affected by the heating part of the model, and it is plotted (solid red line) as compared to the total n case (solid black line) in Fig. 8.

It is important to clarify the difference between n_E and the total n with a Fermi-Dirac distribution (dashed black line). Here, n_E uses a fixed $N(E_x,t)$ at $F_0 = 3$ V/nm and the Fermi-Dirac distribution uses $N(E_x,t)$ at $F_0 = 0$ V/nm. The drop below $n = 2$ in the single energy case (dotted black line) near $\lambda = 800$ nm is related to the resonant enhancement discussed earlier in Fig. 4.

It is clear that heating process will reduce n_E because of the electron emission from higher energies due to heating (E_x is higher), and this explains the multiphoton emission process does require fewer photons because of heating. However, there are photons being absorbed at different energy levels, instead of heating the metal, and thus n_H increases. This combined effect explains why there is not a significant difference in the

total n for the multiphoton emission process as presented in in Fig. 8 (compare the solid and dashed black lines).

We can also use the calculated n and n_E values to determine the average number of photons absorbed (n_H) for heating purposes at different wavelengths, which is $n_H = n - n_E$. For the heating case (solid black line), we have $n = 2$ to 3, and $n_E = 1.75$ to 2, which gives $n_H = n - n_E = 2 - 1.75 = 0.25$ (at small λ) to $n_H = n - n_E = 3 - 2 = 1$ (at large λ) over the range shown in Fig. 8. For the Fermi-Dirac case (dashed black line), we have $n = n_E$ and $n_H = 0$ (no heating included in the model).

Our findings show that the detailed mechanism (either hearing or pure multiphoton absorption) of electron photoemission cannot be completely understood just by plotting the $\sigma \propto F_0^{2n}$ to determine the n. By measuring this n experimentally, we are not able to separate the emission process, namely, the traditional multiphoton emission (no heating) and heating mechanism or in between. To have better characterization of the emission process, it is important also to measure the emission energy spectrum as performed by others[5,9] in addition to the $\sigma \propto F_0^{2n}$ measurement. For example, our Fig. 5 has shown the calculated results to indicate the energy levels of the emitted electrons.

Prior experimental results had reported measured data in the form of a peak-to-baseline ratio, which is defined as the ratio of the total photoemitted charge at $F_0 = F_{\text{peak}} = 2 \times F_{\text{base}}$ to twice the emission at $F_0 = F_{\text{base}}$. The details can be found in Hommelhoff *et al.*[3] In Fig. 9, we compare our results (solid line) with the published measured data (symbols) by using a value of $F_{\text{base}} = 0.3$ V/nm. Comparison with our prior models[13,15] and simplfied model[3] are also presented. Compared to the experimental data (symbols), the pure optical tunneling model (black dashed-dotted line),[13] the pure heating model[15] (red dotted lines), and the combined models in this paper (black solid line) are fairly accurate for $F_{\text{dc}} > 1$ V/nm. This is expected as the effect of the laser field is not important in this high dc field regime. At lower F_{dc} for which the effect of the laser field is important, however, the pure optical tunneling model (black dash-dotted line) underestimates the nonlinearity of the emission process and the pure heating model (red dotted line) overestimates it. The combined model (black solid line) is found to lie between these two models and thus provides a better agreement with the experimental data. It is important to note that our model (solid line) is better than the a simplified model (blue dashed line) that had used $F_{\text{base}} = 2.7$ V/nm as a best fit to the measurement.[3]

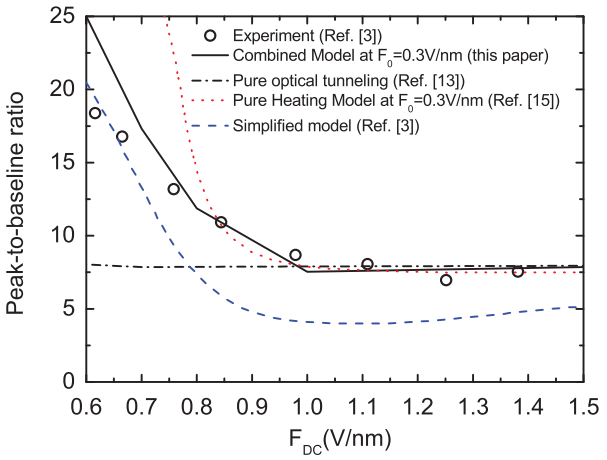

FIG. 9. (Color online) Comparison of the peak-to-baseline ratio from different models with experiment. The circles are experimental results from a previous paper[3] and the blue dashed line is a simplified optical tunneling model (with $F_{\text{base}} = 2.7$ V/nm) from the same paper. The black solid line and the black dash-dotted line represent the result of our combined model and pure optical tunneling model with $F_{\text{base}} = 0.3$ V/nm. The red dotted line is a fit from a pure heating model.[15]

IV. REMARKS

In order to reduce the intense computational requirement, our model assumed an isotropic heating model, which could overestimate the effect of heating and may be responsible for the slightly higher nonlinearity in Fig. 9. The accuracy of the model could be improved in the future by improving on this assumption.

Electron-electron interactions have been ignored in the model and it would be interesting to study space charge effects in the emission process. Thermal conduction, diffusion, normal heating of the laser,[22] and absorption due to roughness[23] have also been ignored since these effects occur on a much longer time scale.

Although we have included the effects of field enhancement on our potential by using a spatially dependent electric field, our model is 1D. As mentioned before, while we have taken into account the spatial dependence of the field, the field enhancement due to the tip radius is never explicitly calculated and the input laser field in the model must be linked to the laser power directly. A recent paper[24] has explicitly calculated the field enhancement factor using finite difference time domain simulations and similar simulations could be added to our model to allow us to relate the emission characteristics with the incoming laser power directly rather than with the electric field at the surface. It should be noted that the study[24] has not taken into account the nonequilibrium heating of the metal.

A classical time-independent image charge term has been assumed in our model. A recent study has introduced a formulation for the time-dependent image charge[25] which is beyond the scope of this paper. However, it would be of interest to study the impact of a time-dependent image charge potential in future studies. Finally plasmonic effect can be included as well.

V. SUMMARY

In summary, we have developed a much improved and more consistent model for ultrafast-laser-induced photoemission in order to account for the effects of nonequilibrium heating, time-dependent quantum tunneling, and multiple energy emission. Using this model, we observe an enhanced emission due to the tranmission resonance at a particular energy level with a barrier height that produces a resonant frequency near the laser frequency. The role of photons in the multiphoton electron emission regime is also studied in details. The model is able to provide a better agreement with experimental data. Smooth transition from the multiphoton regime to the optical tunneling regime is demonstrated. Using this model, the transition based on Einstein generalized photoelectric effect from two-photon to three-photon electron emission is no longer valid.

ACKNOWLEDGMENTS

This work was supported by Singapore MOE (Grant No. 2008-T2-01-033), SUTD (Grant No. SRG EPD 2011 014), and SUTD-MIT IDC (Grants No. IDG21200106 and No. IDD21200103). L.K.A. would like to acknowledge the support of USA AOARD (Grant No. 11-4069).

*ricky_ang@sutd.edu.sg

[1] J. Kupersztych and M. Raynaud, Phys. Rev. Lett. **95**, 147401 (2005).
[2] P. Hommelhoff, Y. Sortais, A. Aghajani-Talesh, and M. A. Kasevich, Phys. Rev. Lett. **96**, 077401 (2006).
[3] P. Hommelhoff, C. Kealhofer, and M. A. Kasevich, Phys. Rev. Lett. **97**, 247402 (2006).
[4] C. Ropers, D. R. Solli, C. P. Schulz, C. Lienau, and T. Elsaesser, Phys. Rev. Lett. **98**, 043907 (2007).
[5] H. Yanagisawa, C. Hafner, P. Dona, M. Klockner, D. Leuenberger, T. Greber, M. Hengsberger, and J. Osterwalder, Phys. Rev. Lett. **103**, 257603 (2009).
[6] M. Schenk, M. Krüger, and P. Hommelhoff, Phys. Rev. Lett. **105**, 257601 (2010).
[7] R. Bormann, M. Gulde, A. Weismann, S. V. Yalunin, and C. Ropers, Phys. Rev. Lett. **105**, 147601 (2010).
[8] M. Krüger, M. Schenk, and P. Hommelhoff, Nature (London) **475**, 78 (2011).
[9] H. Yanagisawa, M. Hengsberger, D. Leuenberger, M. Klockner, C. Hafner, T. Greber, and J. Osterwalder, Phys. Rev. Lett. **107**, 087601 (2011).
[10] C. Kealhofer, S. M. Foreman, S. Gerlich, and M. A. Kasevich, Phys. Rev. B **86**, 035405 (2012).
[11] G. Herink, D. R. Solli, M. Gulde, and C. Ropers, Nature (London) **483**, 190 (2012).
[12] S. V. Yalunin, M. Gulde, and C. Ropers, Phys. Rev. B **84**, 195426 (2011).
[13] M. Pant and L. K. Ang, Phys. Rev. B **86**, 045423 (2012).
[14] L. D. Pietanza, G. Colonna, S. Longo, and M. Capitelli, Eur. Phys. J. D **45**, 369 (2007).
[15] L. Wu and L. K. Ang, Phys. Rev. B **78**, 224112 (2008).
[16] W. Li and L. E. Reichl, Phys. Rev. B **60**, 15732 (1999).
[17] M. Dörr, R. M. Potvliege, D. Proulx, and R. Shakeshaft, Phys. Rev. A **42**, 4138 (1990).
[18] C. Y. Tang, H. C. Bryant, P. G. Harris, A. H. Mohagheghi, R. A. Reeder, H. Sharifian, H. Tootoonchi, C. R. Quick, J. B. Donahue, S. Cohen, and W. W. Smith, Phys. Rev. Lett. **66**, 3124 (1991).
[19] J. G. Fujimoto, J. M. Liu, E. P. Ippen, and N. Bloembergen, Phys. Rev. Lett. **53**, 1837 (1984).
[20] B. Rethfeld, A. Kaiser, M. Vicanek, and G. Simon, Phys. Rev. B **65**, 214303 (2002).
[21] B. Barwick, C. Corder, J. Strohaber, N. Chandler-Smith, C. Uiterwaal, and H. Batelaan, New J. Phys. **9**, 142 (2007).
[22] J. H. Betchel, J. Appl. Phys. **46**, 1585 (1975).
[23] L. K. Ang, Y. Y. Lau, R. M. Gilgenbach, and H. L. Spindler, Appl. Phys. Lett. **70**, 696 (1997).
[24] G. Wachter, C. Lemell, J. Burgdörfer, M. Schenk, M. Krüger, and P. Hommelhoff, Phys. Rev. B **86**, 035402 (2012).
[25] R. D. Muiño, D. Sánchez-Portal, V. M. Silkin, E. V. Chulkov, and P. M. Echenique, Proc. Natl. Acad. Sci. USA **108**, 971 (2011).